Bulk Li mobility enhancement in Spark Plasma Sintered Li(7–3x)AlxLa3Zr2O12 garnet

Adriana Castillo, Thibault Charpentier, Olivier Rapaud, Nicolas Pradeilles, Saïd Yagoubi, Eddy Foy, Mélanie Moskura, Hicham Khodja

Bulk Li mobility enhancement in Spark Plasma Sintered $Li_{(7-3x)}Al_xLa_3Zr_2O_{12}$ garnet

Adriana Castillo[1], Thibault Charpentier[1], Olivier Rapaud[2], Nicolas Pradeilles[2], Saïd Yagoubi[1], Eddy Foy[1], Mélanie Moskura[1], Hicham Khodja[1]

[1] NIMBE, CEA, CNRS, Université Paris-Saclay, CEA Saclay, 91191 Gif sur Yvette Cedex, France

[2] IRCER, UMR CNRS 7315, 12 rue Atlantis, 87068 Limoges Cedex, France

Abstract

$Li_{(7-3x)}Al_xLa_3Zr_2O_{12}$ (LLAZO) Al-doped garnets display high ionic conductivity in the range of ~10^{-4} S.cm^{-1} at room temperature and are thus envisioned for future solid-state batteries. In this study, LLAZO powders with two doping levels were synthetized using a solid-state route and sintered using Spark Plasma Sintering (SPS). Both pristine and SPS crushed pellet powders were investigated using X-Ray Diffraction (XRD) confirming the formation of the most conducting cubic phase. Ionic conductivity measurements were performed using electrochemical impedance spectroscopy. Li and Al distributions among available sites were identified using Magic Angle Spinning (MAS) Nuclear Magnetic Resonance (NMR) experiments, and Li mobility was explored using ^{7}Li static wideline NMR spectroscopy. Results show that SPS treatment, beyond producing highly densified pellets, mainly modifies Al distribution and strongly impacts the bulk Li^+ mobility.

Keywords: Al-doped garnet; NMR; bulk Li^+ mobility; Li dynamics.

1. Introduction

Al-doped garnets $Li_{(7-3x)}Al_xLa_3Zr_2O_{12}$ are characterized by a high ionic conductivity in the range of ~10^{-4} $S.cm^{-1}$ at room temperature and a good electrochemical stability with many electrode materials [1, 2]. They are therefore envisioned as promising electrolyte material for all-solid-state batteries. By introducing more vacancies in the Li sublattice, aliovalent Al^{3+} doping helps stabilize the more conducting cubic polymorph (*Ia-3d*) at room temperature compared to the tetragonal polymorph ($I4_1/acd$) of $Li_7La_3Zr_2O_{12}$ (LLZO) [1, 3– 5].

Within the cubic LLZO structure, Li^+ ions occupy the 24d tetrahedral sites and 48g/96h octahedral sites which are connected with each other by face sharing (see Fig. 1) [1, 6]. Due to partial occupancy of identified Li sites, the diffusion of Li^+ occurs by a concerted migration mechanism [4, 7, 8], and the Li content and its distribution among 24d and 48g/96h sites affects the activation energy of the diffusion process [9].

DFT calculations have shown that the most energetically favorable locations of Al^{3+} dopant in the cubic LLAZO structure are the two 24d and 48g/96h Li sites [10]. Therefore, one may wonder how Al^{3+} substitution at Li sites can impact the diffusion pathways of Li^+ and its mobility.

Several studies have used NMR spectroscopy to investigate Li structural environment and dynamics in tetragonal LLZO [11] and Al-doped (0.9 wt.% and 1.1 wt.%) cubic LLAZO [12, 13]. Site occupancies in the prepared LLAZO were identified using ^{27}Al and ^{6}Li MAS NMR [1, 14–16]. NMR relaxation time measurements allowed getting Li dynamics parameters, namely the Li mean jump rate and activation energy [11, 12]. Microscopic Li dynamics deduced from NMR experiments were also compared with ionic conductivity measurements. The latter, obtained by impedance spectroscopy, reflect Li dynamics only at a macro-scale,

but both methods were found to be in good agreement [11]. However in the studies mentioned above, the occupancy of sites was not correlated with Li dynamics.

Dense pellets are required to increase the ionic conductivity as the detrimental effect of porosity is minimized. Among sintering methods, Spark Plasma Sintering is a very efficient technique to sinter garnets as it produces high density pellets (> 95% of the theoretical density) in a short time (< 10 min), avoiding further material degradation reactions at high temperature and grain growth [17, 18].

In this work, we have studied for two Al-doped garnet powders how SPS treatment modifies Li and Al sites occupancies. Using NMR techniques and impedance spectroscopy measurements we also determined to what extend it impacts the Li dynamics.

2. Sample preparation

2.1. Powder synthesis

LLAZO powders were prepared by conventional solid-state method using Li_2CO_3 (99.997%, Aldrich), Al_2O_3 (99.998%, Aldrich), ZrO_2 (99.978%, Alfa) and La_2O_3 (99.999%, Aldrich) precursors. A 15% Li_2CO_3 excess was added to compensate for Li volatilization at high temperature. Al_2O_3, La_2O_3 and ZrO_2 were dried at 900 °C for 12 h and Li_2CO_3 at 120 °C before weighing. Each mixture was initially calcined at 450 °C in molybdenum crucible, milled using a planetary ball-miller with agate balls in an agate bowl for 4 hours, then transferred in alumina crucible for a treatment at 800 °C overnight. A second ball-milling process was applied with similar conditions before a final calcination at 900 °C during 50 hours under dry air to obtain the pure cubic garnet phase, free from $La_2Zr_2O_7$ intermediate phase. Two powders with different Al content were prepared, the expected Li:Al:La:Zr molar ratios were 54.51:2.08:26.04:17.36 and 51.65:3.04:26.04:17.36 (thereafter referred as S1 and S2 respectively).

2.2. SPS sintering

Powders were sintered without any additives using a Spark Plasma Sintering apparatus (Fuji Syntex, Dr Sinter 825, Japan) under dynamic vacuum. The powders were poured into a graphite die with an inner diameter of 16.4 mm. A compressive graphite foil (0.2 mm thick, Papyex©, Mersen Goup, France) was used as lubricant to coat the inner surface of the die and the surface of the punches. The powders were heated under vacuum up to 1050 °C for 10 minutes with a heating rate of 100 °C/min. A uniaxial pressure of 75 MPa was applied upon heating. Cooling rate was 50 °C/min. Two pellets were produced based on the S1 and S2 powders, named S1-SPS and S2-SPS. The pellets were slightly polished to remove Papyex and possible $La_2Zr_2O_7$ impurity. The latter can form during the sintering process at the interface between the graphitic sheet and the powder due to the high reactivity between lithium and carbon at high temperature inducing Li_2CO_3 formation and consequently leading to a loss of Li from the garnet structure [19, 20].

The pellets density was determined by weighing the pellets on a microbalance and measuring the pellets dimensions with a caliper.

To avoid moisture and CO_2 exposure, all powders and pellets were stored in an Ar-filled glovebox, and air exposure was limited as much as possible.

2.3. Characterization methods

Li, Al, La and Zr concentrations in powders and pellets were measured by Inductive Coupled Plasma (ICP) Optical Emission Spectroscopy (OES) (Varian VistaPro spectrometer).

The structural characterization of the powders and sintered samples was performed by X-ray powder diffraction (XRD) using a Bruker AXS D8 Advance diffractometer equipped with a Lynxeye XE-T linear detector (Cu-$K_{\alpha 1,2}$ radiations) in the Bragg-Brentano configuration. The patterns were acquired at room temperature with 2θ ranging from 10° to 120° (5 s-0.01°

steps). The JANA2006 software [29] was used for structural refinement of the powder X-ray data. The profile was described by a pseudo-Voigt function and a polynomial background was refined in addition to the manual one. Berar-Baldinozzi method was used for the peak shape asymmetry.

The microstructure of the pellets was observed using Scanning Electron Microscopy (JEOL JSM-7001F) with an acceleration voltage of 15 kV.

Electrochemical Impedance Spectroscopy (EIS) measurements were carried out using a Bio-Logic MTZ-35 on polished and gold sputtered pellets in the frequency range of 1 Hz-10 MHz under Ar atmosphere and at temperatures ranging from room temperature to 227 °C.

^{6}Li and ^{27}Al solid-state MAS NMR spectra were collected on a Bruker AVANCE II solid-state NMR spectrometer operating at a magnetic field of 11.72 T (500WB) using 4 mm rotors and a Bruker probe at a sample spinning frequency of 12.5 kHz. Larmor frequencies of ^{6}Li and ^{27}Al were 73.47 MHz and 130.08 MHz, respectively. Chemical shifts were referenced against external aqueous solutions of 1M $AlCl_3$ (0 ppm) and 1M LiCl (0 ppm). For ^{6}Li, additional data were collected at a higher magnetic field of 20 T (850WB) to obtain a better resolution at 10 kHz spinning frequency.

^{27}Al (I = 5/2) MAS NMR spectra were acquired using a single short pulse excitation (1 μs, tip angle of ~15°) to ensure quantitativeness (i.e., working in the non-selective linear regime at short pulse length for quadrupolar nuclei). For ^{6}Li (I = 1), due to the very long nuclear spin-lattice relaxation time, a pre-saturation period followed by a recovery delay (200 s) was systematically employed before a single pulse excitation.

For Li dynamics investigation, ^{7}Li (I = 3/2) wideline (i.e., non-spinning) NMR spectra and nuclear relaxation measurements were acquired at a Larmor frequency of 116.4 MHz on a

Bruker AVANCE I spectrometer operating at a magnetic field of 7.02 T (300WB) using a variable temperature wideline probe in the -123 °C – 227 °C range. For lower temperatures (down to -183 °C), data were collected using an Oxford Spectrostat NMR system cooled with liquid nitrogen.

3. Results and discussion

3.1. Structural arrangement and evolution after SPS treatment

S1, S2, and crushed S1-SPS and S2-SPS powders were investigated by XRD in order to confirm the cubic phase formation and to identify possible modifications after SPS treatment.

The XRD patterns of the two pristine samples S1 and S2 are unambiguously indexed with the garnet cubic phase (*Ia-3d*) (ICSD #238688) as shown in Fig. 2.

As Al^{3+} ionic radius is smaller than Li^{+} (39 pm vs. 59 pm) a lattice parameter decrease is expected with increasing the doping level. From le Bail refinements (see example in Fig. S1), we found a smaller lattice parameter for S2 (12.9870(6) Å) compared to S1 (13.0124(4) Å) confirming the unit cell shrinkage and its correlation with the Al^{3+} content. In the two pristine samples S1 and S2, $LaAlO_3$ impurity was found in XRD patterns and confirmed by ^{27}Al MAS NMR (see below). Moreover we suspected the existence of a second impurity $Li_{1.82}ZrO_3$ (ICSD #35236) on the pristine samples, which main reflection (021) is observed around 26.76°. However, we noticed the disappearance of impurity reflections after the SPS treatment and no modification of the LLAZO cubic phase as illustrated on Fig. 2. Moreover a decrease in the unit cell parameters was observed in the SPS sintered samples (Table S1) compared to the pristine powders (13.0124 Å and 12.9758 Å for S1 and S1-SPS, 12.9870 Å and 12.9634 Å for S2 and S2-SPS). This suggests that the removal of $LaAlO_3$ after sintering could result from the insertion of further Al ions in the garnet structure.

3.2. Elemental compositions and microstructures of powders and pellets

Elemental compositions from ICP-OES analyses are reported in Table 1. As oxygen concentration cannot be measured by ICP analysis, results are expressed as the ratio of elemental concentrations normalized to the sum of Li, Al, Zr and La concentrations. Importantly, concentrations in the garnet phase were deduced after removal of the $LaAlO_3$ parasitic phase contribution, estimated from ^{27}Al MAS NMR as explained in section 3.3. With SPS treatment, Al content has increased in the two pellets as suggested by XRD analysis.

In Figure 3 we show backscattered SEM images of S1 and S2 powders and front views of S1-SPS and S2-SPS polished pellets. Grain sizes range from 2 to 10 µm and the two pellets seem well sintered with little porosity. The measured relative densities of SPS-sintered pellets are 91% for S1-SPS (4.8 $g.cm^{-3}$) and 96% for S2-SPS (5.1 $g.cm^{-3}$). Minor darker zones are visible on the SEM images indicating the existence of a lighter phase as $LaAlO_3$ impurity.

3.3. Ionic conductivity

The ionic conductivities of the two sintered pellets were measured by EIS. An example of the Nyquist diagram obtained at 44 °C for S1-SPS is shown on Fig. 4a while Arrhenius plots for both samples are displayed on Fig. 4b. The high frequency part of the EIS spectrum showing a half circle was attributed to the electrolyte response and the low frequency region was associated to the electrode/electrolyte interface contribution. As responses of both the bulk and the grain boundaries are probably in the same frequency range, the two contributions cannot be separated and solely the total ionic conductivity was reported.

At room temperature we measured total conductivities $\sigma_{Total} = 1.6 \times 10^{-4}$ $S.cm^{-1}$ and 0.9×10^{-4} $S.cm^{-1}$ for S1-SPS and S2-SPS respectively, comparable to the ones reported in literature [17, 21]. Activation energies (E_a) extracted from Arrhenius plots were E_a = 0.46 eV and 0.42 eV for S1-SPS and S2-SPS, respectively, slightly higher than reported values [3, 12, 15].

However our values are probably reflecting the global activation energy, increased by the contribution of the less conductive $LaAlO_3$ impurity. Similarly, Yamada et al. [17] measured a higher activation energy for grain boundaries (0.453 eV) compared to bulk (0.364 eV).

3.4. Microscopic Li dynamics

To get more insight into microscopic Li dynamics of the LLAZO pellets, we performed ^{7}Li wideline NMR experiments between -123 and 227 °C.

For all samples, the linewidth obtained from spectrum deconvolution (see Fig. S2) decreased with temperature as shown on Fig. 5. This so-called motional narrowing occurring during sample heating reflects the faster Li^+ ions diffusion in the structure as the temperature increases, thus averaging effects of local fields (^{7}Li-^{7}Li dipolar and ^{7}Li quadrupolar interactions). The onset temperature of the motional narrowing process denoted T^{MN} (i.e. the temperature corresponding to the inflexion point) is the relevant information and can be linked to the activation energy of the Li hopping process by the empirical expression of Waugh and Fedin [11]:

$$E_a = 1.617 \times 10^{-3} \times T^{MN}(K) \qquad (1)$$

Moreover, motional narrowing experiments give also access to an estimate of the mean Li jump rate (τ^{-1}) at T^{MN}, using the relation:

$$\tau^{-1} \sim 2\pi\Delta\delta_0 \qquad (2)$$

with $\Delta\delta_0$ representing the central line width at the inflexion point [11, 12].

Importantly, we observed a significant shift of the onset temperature T^{MN} toward lower temperatures after SPS treatment for both crushed pellets. The onset temperature was lowered by 130 K for S1 and 100 K for S2 after SPS. Following equation (1) this implies that the activation energy for Li motion decreases by approximatively one third of its value after SPS

treatment, and using equation (2), that higher temperature is needed to reach a mean Li jump rate of ~ 10^4 s^{-1} in powders compared to SPS sintered samples. It is worth noting that comparable values of T^{MN} were observed for S1-SPS and S2-SPS samples, reflecting equivalent Li dynamics in both sintered samples. This is probably related to the similar Li and Al distributions found for both samples after SPS treatment as shown in the next section.

3.5. Li^+ and Al^{3+} site occupancies investigated by MAS NMR

Li^+ and Al^{3+} site occupancies were obtained through ^6Li and ^{27}Al MAS NMR spectra analysis on S1 and S1-SPS (Fig. 6) and S2 and S2-SPS (Fig. 7).

Two peaks are expected in ^6Li MAS NMR spectra of garnet samples from the literature [9]. A first peak was observed at around 0.1 ppm which is attributed to Li located in the 24d tetrahedral sites of the garnet structure while a second peak at ~1.2 ppm is attributed to 48g/96h octahedral sites [9]. Measurements at very-high field (20 T) allowed collection of highly resolved ^6Li MAS NMR spectra as shown on Fig. 6. Deconvolution of Li band in Fig. S3 provided the site distribution, reported in Table 2. Similar ratio were found for all powders and SPS samples with around 10% of Li located in 24d sites and 90% in 48g/96h sites. This result shows that SPS did not modify Li distribution among sites. However, a clear narrowing in the peak widths was observed in SPS samples spectra which indicates an increase of Li mobility.

^{27}Al MAS NMR spectra are displayed in Fig. 7. In the literature [1, 14, 15], the two peaks at ~70 ppm and ~82 ppm are attributed to Al^{3+} located in the 24d sites and 48g/96h sites in the garnet phase respectively, 48g and 96h being unresolved as they are neighbor sites (see Fig. 1) [10]. Even though highly distorted 96h sites have an approximate 5-fold coordination number, the value of the isotropic chemical shift suggests that Al ions adopt locally a different coordination geometry than that of Li ions in these sites (4-fold coordination number)[1].

In order to fit the ^{27}Al MAS NMR spectra, MQMAS experiments were performed to obtain better information of the NMR parameters. As shown in Fig. S5, the two-dimensional spectra clearly revealed a distribution of the NMR parameters, mostly for the isotropic chemical shift. Such a dispersion can be ascribed to the local disorder in terms of Li sites occupancies. Additional MAS NMR experiments at high temperature showed indeed a narrowing when increasing the temperature (data not shown). Here, it was found that using a distribution of NMR parameters chosen as a product of three Gaussian distributions $\pi(\delta_{iso},C_Q,\eta)=G(\delta_{iso})\times G(C_Q)\times G(\eta)$ yielded a very satisfactory fit of the MQMAS spectra as shown in Fig. S6. The NMR parameters were then allowed to vary within 10% from the obtained values to fit the MAS spectra.

We report in Table S2 the mean and standard deviation value of each NMR parameters, namely the quadrupolar coupling constant C_Q, the quadrupolar asymmetry parameter η and the isotropic chemical shift δ_{iso}.

The low asymmetry parameter (η = 0.2) found for all samples for the 70 ppm peak is consistent with the axial symmetry of tetrahedral 24d sites. η is higher for the 82 ppm peak (η ~ 0.9) which is more consistent with 48g/96h sites where Al^{3+} ions can be as well on a centered or on an off-centered position depending on the repulsion interactions with neighboring ions (Li^+ and Al^{3+}) [10]. In ^{27}Al MQMAS NMR experiments conducted at room temperature no other sites were detected (see Fig. S5).

In Fig. 7 we observed a third peak at 12 ppm which is attributed to Al in the $LaAlO_3$ impurity phase [10, 12]. It can be noticed that after SPS this peak was strongly lowered for both samples (Table 2). This is consistent with XRD observations and suggests again that SPS promoted conversion of $LaAlO_3$ into LLAZO and thus Al insertion in the garnet structure.

From our experimental spectra, occupancy of Al^{3+} sites in the garnet phase was further estimated after removal of the $LaAlO_3$ contribution. It was found for S1 that nearby all Al^{3+}

ions were located on 24d sites whereas they were distributed in S2 between both sites, 34% located in 48g/96h sites and 66% in 24d sites (Table 2).

NMR clearly shows that Al ion distribution is significantly modified after SPS for both doped samples. For S1-SPS, data show that nearby 20% of Al^{3+} ions moved from 24d to 48g/96h sites. For S2-SPS, the Al^{3+} occupancy of 48g/96h sites decreased to 11% and Al^{3+} occupancy of 24d sites increased to 89%. Al distribution is therefore considerably affected by SPS treatment contrary to what was observed for Li^{+}.

The location of Al^{3+} ions impacts the Li mobility as Coulombic repulsions induced by Al^{3+} ions block surrounding sites for Li hops. When Al occupies a 24d site, four octahedral (48g/96h) sites are blocked while when Al is located on a 48g/96h site only two 24d sites are blocked [22]. Interestingly we noticed that after SPS treatment the resulting Al distribution among sites were similar for both powders (~85 % in 24d and ~15% in 48g/96h sites).

From the measured Al and Li relative occupancies and composition data from ICP, knowing the structural data of cubic garnet crystallographic phase, an attempt was made to calculate the remaining proportion of vacancies on each site. It should however only being considered as an estimate and DFT calculations would help at clarifying the 48g/96h effective site splitting. We considered here that two Al^{3+} or one Al^{3+} and one Li^{+} cannot simultaneously occupy neighboring 48g and 96h sites because of high Coulombic repulsion due to short distance between 48g and 96h sites. Therefore, our calculations considered 96h/48g/96h as a single site. The results are presented in Fig. 8, and confirm the strong similarity between the two powders following SPS treatment.

Very little vacancies were found for 48g/96h octahedral sites in both samples (< 3%), whereas a majority of vacancies were located on the 24d tetrahedral sites (~ 70%). These site occupancies are consistent with Figure 5 of [23].

To sum up, we showed that the SPS treatment leads to (i) a strong reduction of $LaAlO_3$ impurity, (ii) Al inclusion in the garnet phase, (iii) a redistribution of Al ions among available sites and (iv) a significant lowering of the motional narrowing onset temperature. We therefore infer that SPS, besides being a fast and extremely performant densification process, induces profound modifications in the sintered material. The combination of all the effects mentioned above are responsible for the increased ion mobility in the SPS-sintered Al-doped garnets.

Moreover, even though the Al content increased in the samples after SPS treatment (section 3.2), it should not be considered as the main reason for the great enhancement in Li mobility since S1 has a similar Al content compared to S2-SPS but not such high Li mobility.

Al insertion in the garnet phase and ion redistribution into available sites may be related to an electromigration process during SPS treatment, mainly on Al^{3+} as it is more sensitive to electric fields compared to Li^{+}. Although not reported yet, this process should be correlated to electromigration mitigated effects such as carbon insertion [17], Frenkel pair nucleation [26] or oxygen gradient in UO_{2+x} [27]. Moreover the extremely fast cooling rate used in SPS sintering could have quenched the system into a metastable state with highly disordered ionic distribution, favoring high Li mobility [5, 25, 28–29].

However this assumption would need further investigations through calculations such as ab initio and molecular dynamics to get a deeper understanding on the effect of SPS on ionic distribution. Comparison with hot pressing sintering method could also help at clarifying the SPS effect, even though grain growth will occur due to the longer duration of the sintering process.

Conclusions

In this study, we have prepared cubic LLAZO with two Al doping levels. XRD measurements confirmed the synthesis of the more conducting cubic phase, and following SPS treatment, ionic conductivity measured by EIS on densified pellets was found in the range of ~10^{-4} $S.cm^{-1}$ at 25 °C. ^{27}Al MAS NMR revealed that a redistribution of Al ions between available sites occurred after SPS without affecting the cubic phase as confirmed by XRD. Moreover, by means of temperature-variable ^{7}Li static NMR, it was observed that SPS treatment significantly decreases the motional narrowing onset temperature T^{MN} by ~100 K in comparison with the pristine powders, demonstrating that bulk mobility of Li was strongly enhanced by SPS.

This study reveals that the enhancement of the total ionic conductivity of SPS sintered samples is not only due to a better densification that effectively restrains porosity effect but also results from an increased bulk ionic conductivity caused by modified Al site occupancies that favor higher Li mobility.

These observations should be extended to a wider range of doping levels and various conducting ceramics, and demonstrate also how NMR studies help at understanding the underlying mechanisms of SPS treatment.

Acknowledgments

Authors thanks Junxian Zhang (ICMPE, Thiais, France) for ICP measurements and Enrique Vega (NIMBE, Saclay, France) for SEM. Financial support from the TGIR-RMN-THC Fr3050 CNRS for conducting the ^{6}Li MAS NMR measurements is gratefully acknowledged. Authors are also very grateful to Pierre-Marie Geffroy (IRCER, Limoges, France) for fruitful discussions and Magali Gauthier (NIMBE, Saclay, France) for careful rereading of the text.

Appendix A. Supplementary material

Attached file

References

[1] C. A. Geiger, E. Alekseev, B. Lazic, M. Fisch, T. Armbruster, R. Langner, M. Fechtelkord, N. Kim, T. Pettke, W. Weppner, Crystal chemistry and stability of $Li_7La_3Zr_2O_{12}$ garnet: A fast lithium-ion conductor, Inorg. Chem. 50 (2011) 1089–1097.

[2] R. Murugan, V. Thangadurai, W. Weppner, Fast lithium ion conduction in garnet-type $Li_7La_3Zr_2O_{12}$, Angew. Chem. Int. Ed. 46 (2007) 7778–7781.

[3] Y. Matsuda, K. Sakamoto, M. Matsui, O. Yamamoto,Y. Takeda, N. Imanishi, Phase formation of a garnet-type lithium-ion conductor $Li_{7-3x}Al_x La_3Zr_2O_{12}$, Solid State Ionics 277 (2015) 23–29.

[4] N. Bernstein, M. D. Johannes, K. Hoang, Origin of the structural phase transition in $Li_7La_3Zr_2O_{12}$, Phys. Rev. Lett. 109 (2012) 2–6.

[5] Y. Matsuda, Y. Itami, K. Hayamizu, T. Ishigaki, M. Matsui,Y. Takeda, O.Yamamoto, N. Imanishi, Phase relation, structure and ionic conductivity of $Li_{7-x-3y}Al_yLa_3Zr_{2-x}Ta_xO_{12}$, RSC Adv. 6 (2016) 78210–78218.

[6] Y.Li, J.- T. Hanc, C.- A. Wanga, S. C. Vogelc, H. Xieb, M. Xub, J. B. Goodenough, Ionic distribution and conductivity in lithium garnet $Li_7La_3Zr_2O_{12}$, J. Power Sources 209 (2012) 278–281.

[7] R. Jalem, Y. Yamamoto, H. Shiiba, M. Nakayama, H. Munakata, T.Kasuga, K. Kanamura, Concerted migration mechanism in the Li ion dynamics of garnet-type $Li_7La_3Zr_2O_{12}$, Chem. Mater. (2013) 425-430.

[8] M. Xu, M. S. Park, J. M. Lee, T. Y. Kim, Y. S. Park, E. Ma, Mechanisms of Li + transport in garnet-type cubic $Li_{3+x}La_3M_2O_{12}$ (M = Te, Nb, Zr), Phys. Rev. B - Condens. Matter Mater. Phys. 85 (2012) 1–5.

[9] L. van Wüllen, T. Echelmeyer, H.-W. Meyer, D. Wilmer, The mechanism of Li-ion transport in the garnet $Li_5La_3Nb_2O_{12}$, Phys. Chem. Chem. Phys. 9 (2007) 3298–3303.

[10] D. Rettenwander, P. Blaha, R.Laskowski, K. Schwarz, P. Bottke, M. Wilkening, C. A. Geiger, G. Amthauer, DFT Study of the Role of Al 3+ in the Fast Ion-Conductor $Li_{7-3x}Al_{3+x}La_3Zr_2O_{12}$ Garnet, Chem. Mater. 26 (2014) 2617–2623.

[11] A. Kuhn, S. Narayanan, L. Spencer, G. Goward, V. Thangadurai, M. Wilkening, Li self-diffusion in garnet-type $Li_7La_3Zr_2O_{12}$ as probed directly by diffusion-induced Li7 spin-lattice relaxation NMR spectroscopy, Phys. Rev. B - Condens. Matter Mater. Phys. 83 (2011) 1–11.

[12] H. Buschmann, J. Dölle, S. Berendts, A. Kuhn, P. Bottke, M. Wilkening, P. Heitjans, A. Senyshyn, H.Ehrenberg, A. Lotnyk, V. Duppel, L. Kienle, J. Janek, Structure and dynamics of the fast lithium ion conductor $Li_7La_3Zr_2O_{12}$, Phys. Chem. Chem. Phys. 13 (2011) 19378.

[13] A. Kuhn, J.- Y. Choi, L. Robben, F. Tietz, M. Wilkening, P. Heitjans, Li Ion Dynamics in Al-Doped Garnet-Type $Li_7La_3Zr_2O_{12}$ Crystallizing with Cubic Symmetry, Zeitschrift für Phys. Chemie 226 (2012) 525–537.

[14] A. A. Hubaud, D. J. Schroeder, B. Key, B. J. Ingram, F. Dogan, J. T. Vaughey, Low temperature stabilization of cubic $(Li_{7-x}Al_{x/3})La_3Zr_2O_{12}$: role of aluminum during formation, J. Mater. Chem. A 1 (2013) 8813.

[15] Y. Zhang, F. Chen, R. Tu, Q. Shen, X. Zhang, L. Zhang, Effect of lithium ion concentration on the microstructure evolution and its association with the ionic conductivity of cubic garnet-type nominal $Li_7Al0.25La_3Zr_2O_{12}$ solid electrolytes, Solid State Ionics 284 (2016) 53–60.

[16] A. Düvel, A. Kuhn, L. Robben, M. Wilkening, P. Heitjans, Mechanosynthesis of Solid Electrolytes: Preparation, Characterization, and Li Ion Transport Properties of Garnet-type Al-doped $Li_7La_3Zr_2O_{12}$ Crystallizing with Cubic Symmetry, J. Phys. Chem. C 116 (2012) 15192–15202.

[17] H. Yamada, T. Ito, R. Hongahally Basappa, Sintering Mechanisms of High-Performance Garnet-type Solid Electrolyte Densified by Spark Plasma Sintering, Electrochim. Acta 222 (2016) 648–656.

[18] R. Kali and A. Mukhopadhyay, Spark plasma sintered/synthesized dense and nanostructured materials for solid-state Li-ion batteries: Overview and perspective, J. Power Sources 247 (2014) 920–931.

[19] H. Yamada, T. Ito, R. Hongahally Basappa, Sintering Mechanisms of High-Performance Garnet-type Solid Electrolyte Densified by Spark Plasma Sintering, Electrochim. Acta 222 (2016) 648–656.

[20] H. Geng et al., Formation Mechanism of Garnet-Like $Li_7La_3Zr_2O_{12}$ Powder Prepared by Solid State Reaction, Rare Met. Mater. Eng. 45 (2016) 612–616.

[21] M. Botros, R. Djenadic, O. Clemens, M. Möller, H. Hahn, Field assisted sintering of fine-grained $Li_{7-3x}La_3Zr_2Al_xO_{12}$ solid electrolyte and the influence of the microstructure on the electrochemical performance, J. Power Sources 309 (2016) 108–115.

[22] D. O. Shin et al., Synergistic multi-doping effects on the $Li_7La_3Zr_2O_{12}$ solid electrolyte for fast lithium ion conduction, Sci. Rep. 5 (2016) 18053.

[23] V. Thangadurai, S. Narayanan, D. Pinzaru, Garnet-type solid-state fast Li ion conductors for Li batteries: critical review, Chem. Soc. Rev. 43 (2014) 4714.

[24] C. Chen, Z. Lu, F. Ciucci, Data mining of molecular dynamics data reveals Li diffusion characteristics in garnet $Li_7La_3Zr_2O_{12}$, Sci. Rep. 7 (2017) 40769.

[25] K. Meier, T. Laino, A. Curioni, Solid-state electrolytes: Revealing the mechanisms of Li-Ion conduction in tetragonal and cubic LLZO by first-principles calculations, J. Phys. Chem. C 118 (2014) 6668–6679.

[26] M. Cologna, J.S.C. Francis, R. Raj, Field assisted and flash sintering of alumina and its relationship to conductivity and MgO-doping, J. Eur. Ceram. Soc. 31(2011) 2827-2837.

[27] V. Tyrpekl, M. Naji, M. Holzhäuser, D. Freis, D. Prieur, P. Martin, B. Cremer, M. Murray-Farthing, M. Cologna, On the Role of the Electrical Field in Spark Plasma Sintering of UO_{2+x}, Sci. Rep. 7 (2017) 46625.

[28] M. Burbano, D. Carlier, F. Boucher, B. J. Morgan, M. Salanne, Sparse Cyclic Excitations Explain the Low Ionic Conductivity of Stoichiometric $Li_7La_3Zr_2O_{12}$, Phys. Rev. Lett. 116 (2016) 1–6.

[29] V. Petříček, M. Dušek, L. Palatinus, Crystallographic Computing System JANA2006: General features. Z. Kristallogr. - Cryst. Mater. 229 (2014) 345– 352.

Figure captions

Fig. 1. (a) Crystal structure of cubic-type LLAZO (Ia-3d) (ICSD #238690). (b) Li tetrahedral (24d) and octahedral (48g/96h) site connections.

Fig.2*:* X-ray diffraction patterns of S1, S2, S1-SPS and S2-SPS samples collected with Cu-$K_{\alpha 1,2}$ radiations.

Fig. 3: Backscattered SEM images of (a) S1 powder, (b) S2 powder, (c) polished S1-SPS, (d) polished S2-SPS.

Fig. 4. (a) Nyquist plots of S1-SPS impedance at 44°C and equivalent circuit; (b) Arrhenius plot of total ionic conductivity of LLAZO samples.

Fig.5. ^{7}Li NMR full width at half maximum (FWHM) of the central transition versus temperature for both studied compositions.

Fig. 6. Experimental ^{6}Li MAS NMR spectra of the studied samples recorded at 20 T and sample spinning frequency of 10 kHz.

Fig. 7. Experimental ^{27}Al MAS NMR spectra of the studied samples recorded at magnetic field of 11.72 T and sample spinning frequency of 12.5 kHz.

Fig. 8. Relative occupancy of (a) tetrahedral and (b) octahedral sites by Li, Al and vacancies in LLAZO from deconvoluted spectra of ^{27}Al and ^{6}Li MAS NMR

Tables

		S1	S1-SPS	S2	S2-SPS
$LaAlO_3$ phase in the sample (at.%)		5.1(3)	2.9(2)	10.6(6)	1.1(1)
Elemental ratio in the garnet phase (at.%)	**Li**	56(1)	56(1)	57(1)	54(1)
	Al	2.2(1)	2.4(1)	1.5(1)	2.3(1)
	La	25(1)	25(1)	25(1)	26(1)
	Zr	17.2(2)	16.8(3)	16.7(3)	17.4(3)

Table 1. Atomic concentrations (normalized to 100%) of Li, Al, La and Zr in the garnet samples and molar content of $LaAlO_3$ (see text).

Li (at.%)					
		S1	**S1-SPS**	**S2**	**S2-SPS**
Li in 24d sites (0.1ppm)		10	9	10	9
Li in 48g/96h sites (1.2 ppm)		90	91	90	91
Al (at.%)					
		S1	**S1-SPS**	**S2**	**S2-SPS**
Al_{LaAlO3} (12 ppm)		17	9	40	4
In garnet phase	$Al_{LLAZO(24d)}$ (70 ppm)	99	84	66	90
	$Al_{LLAZO(48g/96h)}$ (82 ppm)	1	16	34	10

Table 2. Li and Al locations from ^{6}Li and ^{27}Al MAS NMR spectra. Population error is estimated as 1%.

Figure

Figure 1.

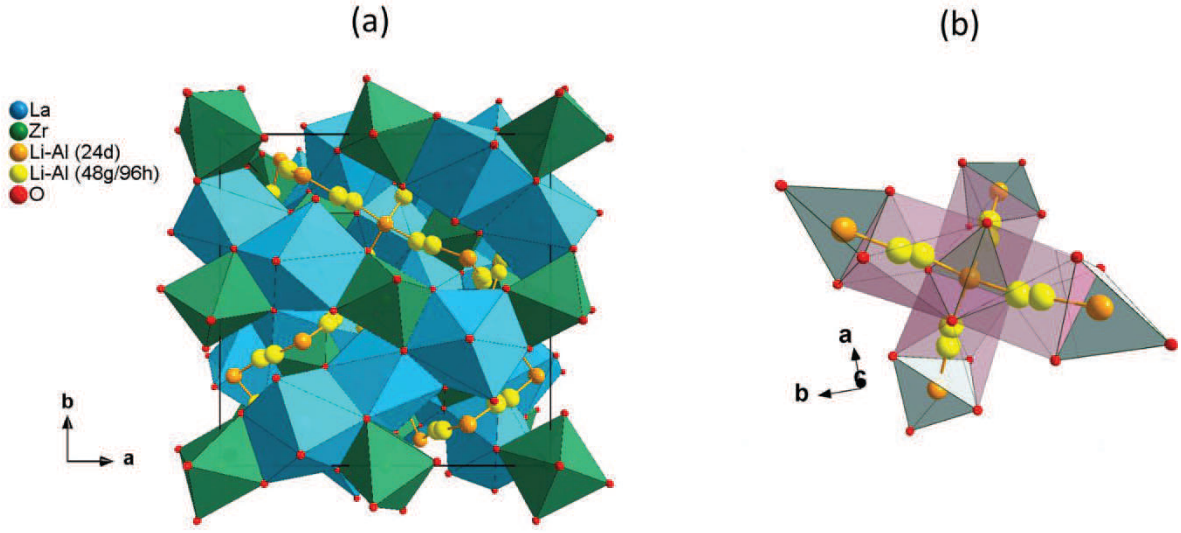

Figure2

Figure 2.

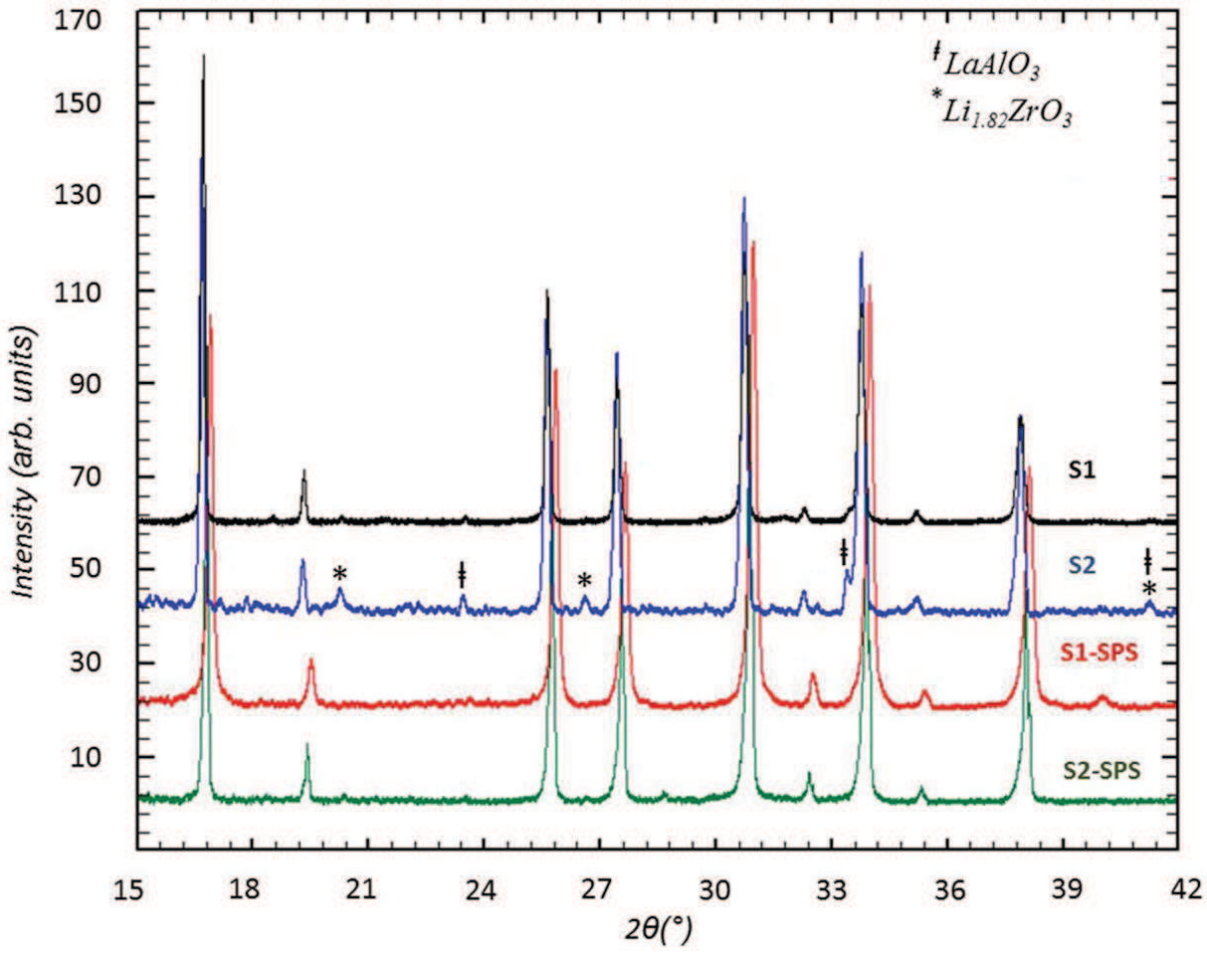

Figure3

Figure 3.

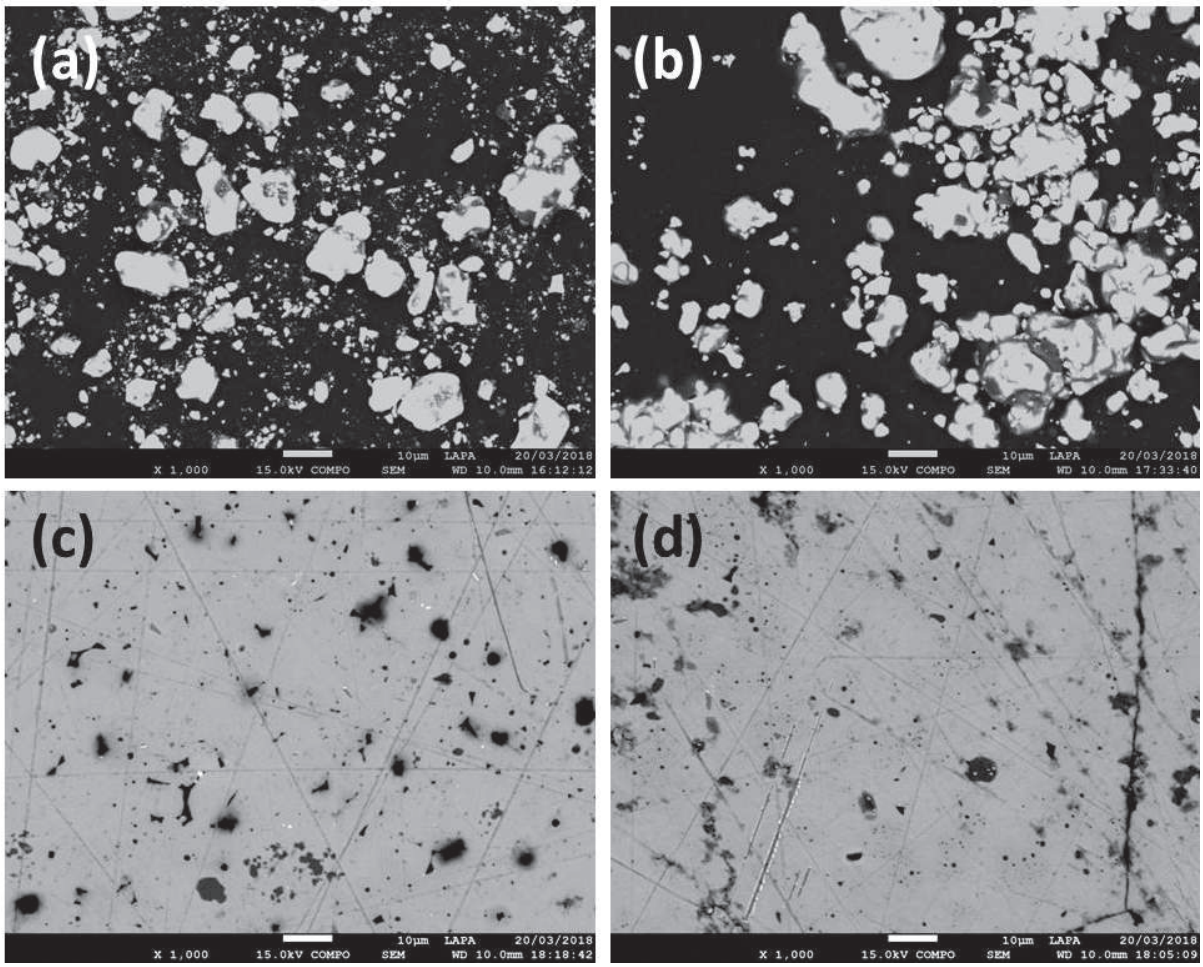

Figure4

Figure 4.

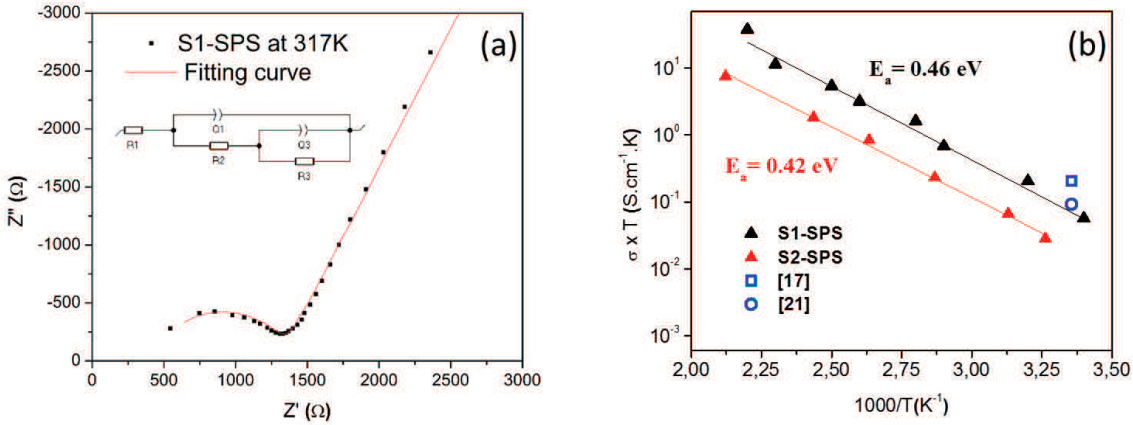

Figure5

Figure 5.

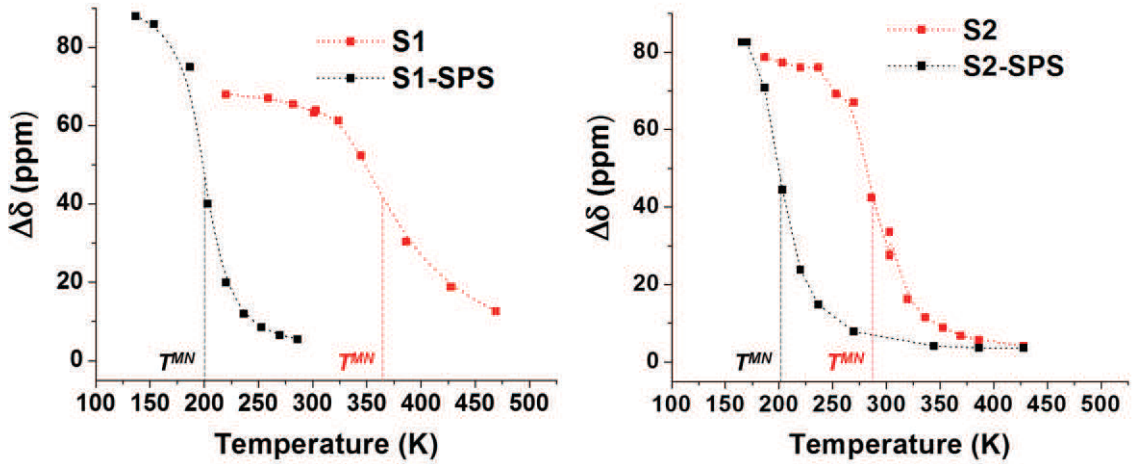

Figure6

Figure 6.

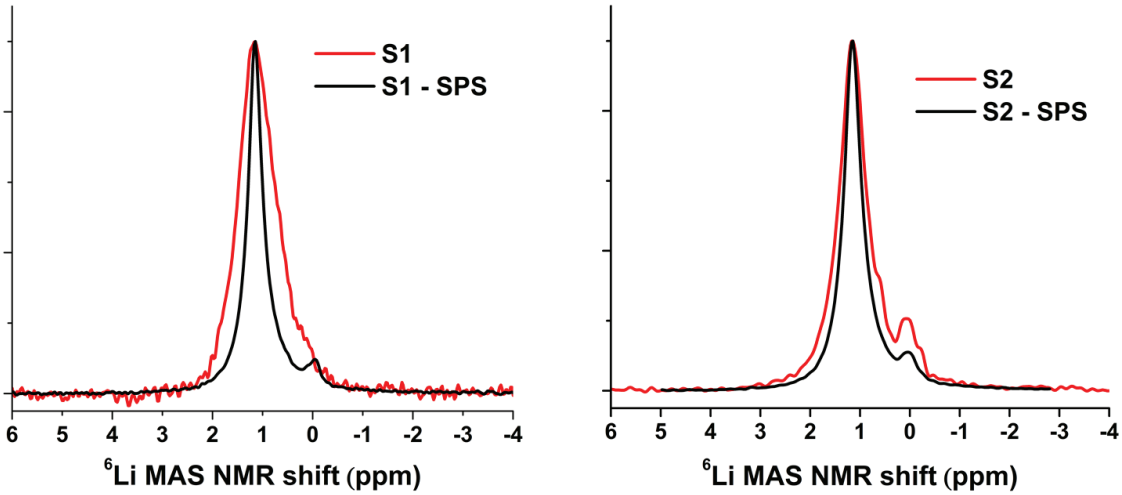

Figure7

Figure 7.

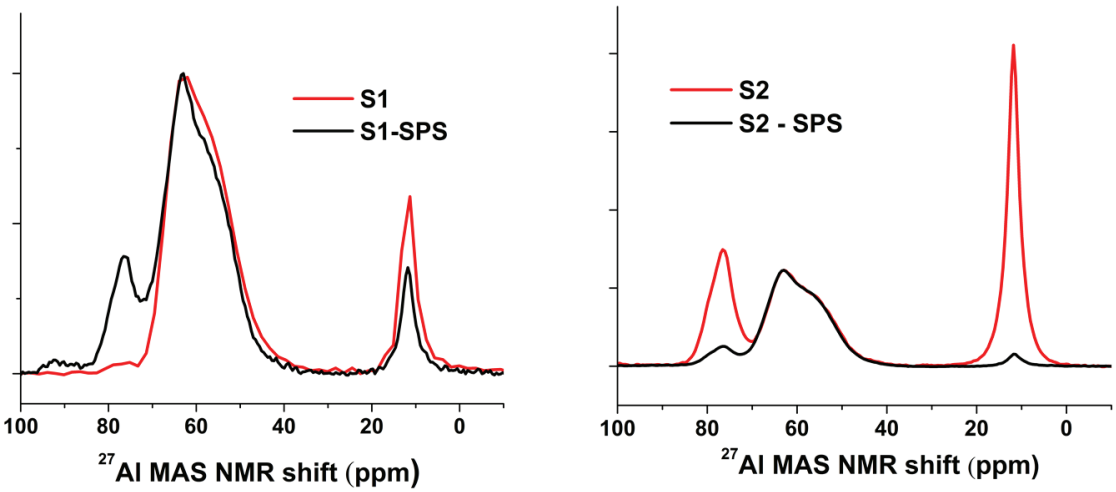

Figure8

Figure 8.

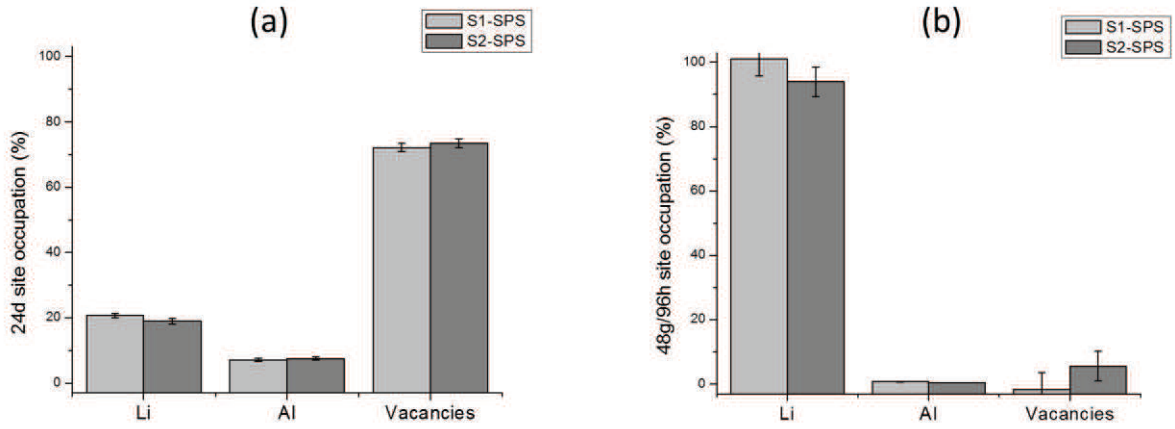

[Supplementary Material]

Bulk Li mobility enhancement following Spark Plasma Sintering on $Li_{(7-3x)}Al_xLa_3Zr_2O_{12}$ garnet revealed by Nuclear Magnetic Resonance

Adriana Castillo, Thibault Charpentier, Olivier Rapaud, Nicolas Pradeilles, Saïd Yagoubi, Eddy Foy, Mélanie Moskura, Hicham Khodja

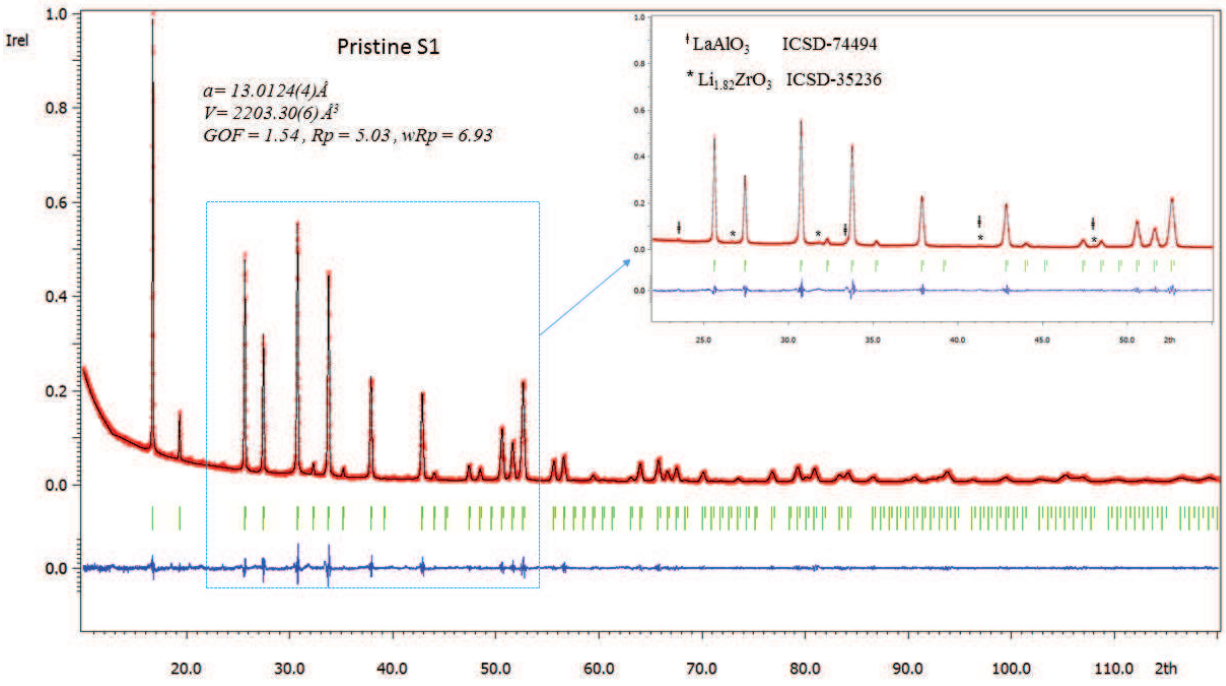

Fig. S1: Calculated scattering intensity profile (black) compared to experimental data (red) for garnet sample S1. For practical reasons, only Lebail refinement for pristine S1 is given.

Sample	***S1***	***S1-SPS***	***S2***	***S2-SPS***
Crystal data				
Crystal symmetry	Cubic			
Space group	I a-3d no (230)			
Unit cell	a = 13.0124(4) Å	a = 12.9758(5) Å	a = 12.9870(6) Å	a = 12.9634(3) Å
Cell volume	V = 2203.30(6) $Å^3$	V = 2184.75(8) $Å^3$	V = 2190.41(9) $Å^3$	V = 2178.52(5) $Å^3$
Z	8	8	8	8
Rp	5.03	4.73	2.57	5.00
wRp	6.93	6.65	3.62	7.37
GOF	1.54	1.33	1.18	1.8

Table S1: Crystal data and structure refinement parameters for LLAZO

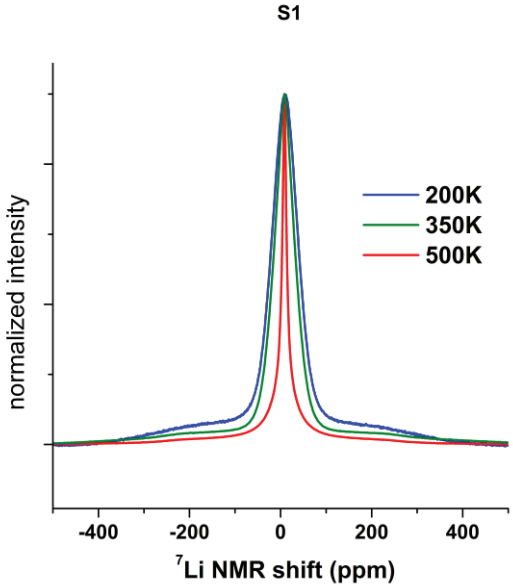

Fig. S2: Experimental ^{7}Li NMR spectra of S1 sample at different temperatures. The spectra are deconvoluted by combining a narrow central line (central transition) and a wider contribution (satellite transitions) with lower intensity.

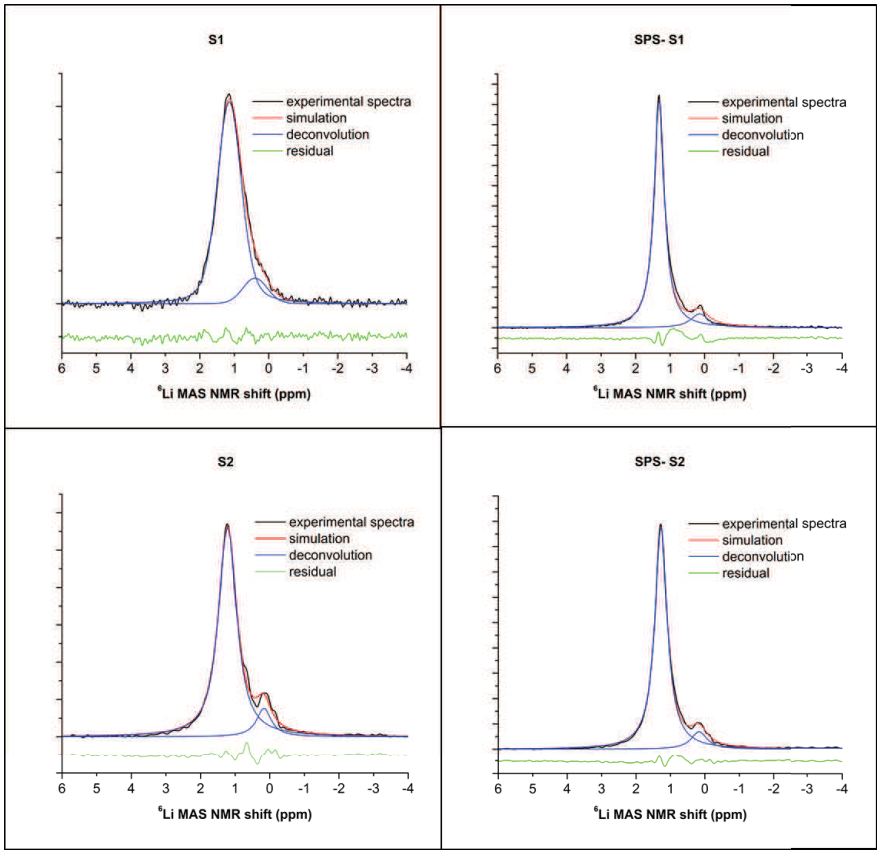

Fig. S3: Experimental and simulated ^{6}Li MAS NMR spectra of the studied samples at room temperature.

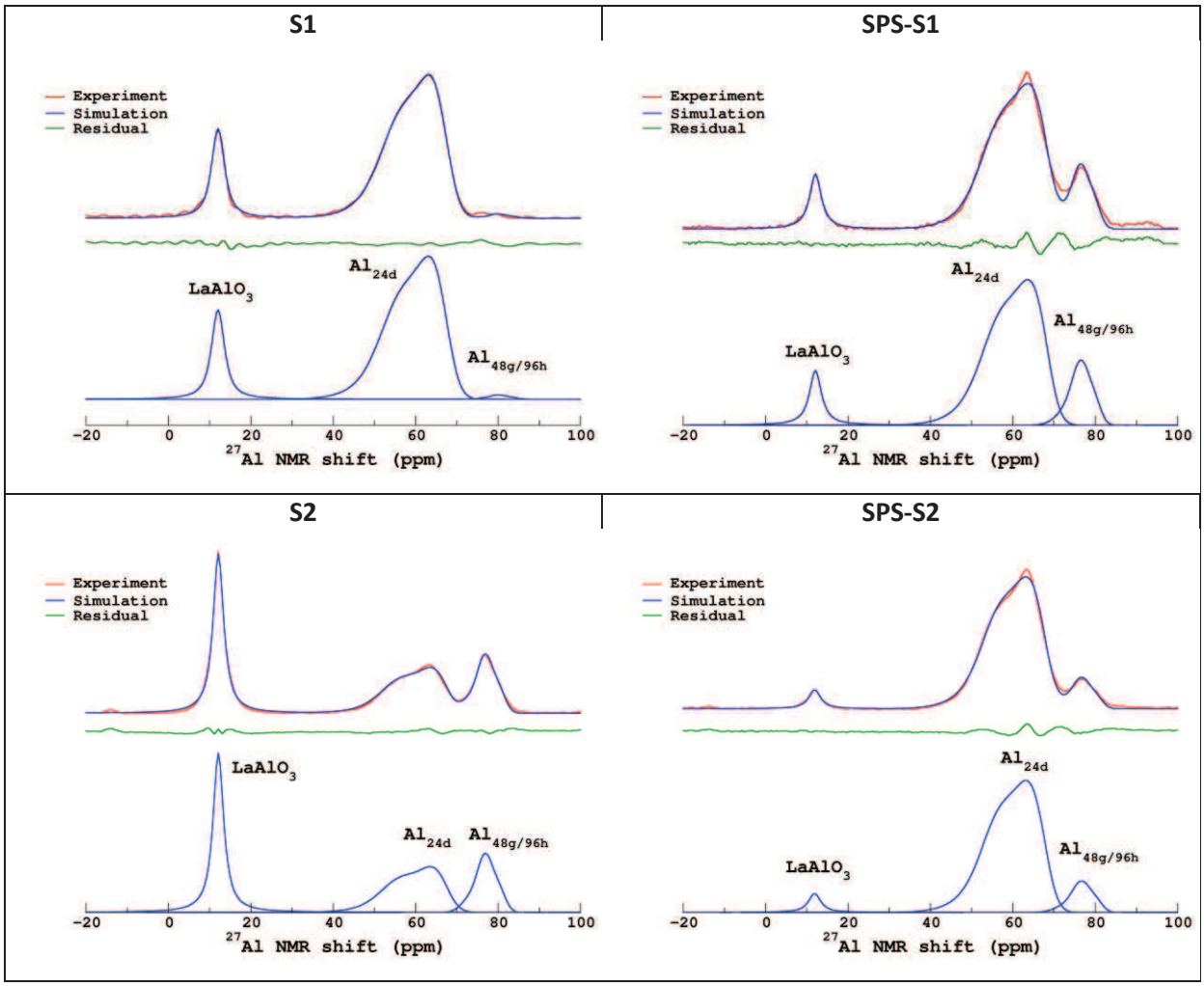

Fig. S4: Experimental and simulated ^{27}Al MAS NMR spectra of studied samples at room temperature.

	$Al_{LLAZO(24d)}$		
	δ_{iso} (ppm)	C_Q (MHz)	η
S1	70.0 (2.5)	5.5 (0.6)	0.2 (0.02)
S1-SPS	70.9 (2.2)	5.5 (0.5)	0.3 (0.01)
S2	70.3 (2.5)	5.5 (0.5)	0.2 (0.02)
S2-SPS	70.2 (2.2)	5.4 (0.5)	0.3 (0.02)

	$Al_{LLAZO(48g/96h)}$		
	δ_{iso} (ppm)	C_Q (MHz)	η
S1	n.a (<1%)	n.a (<1%)	n.a (<1%)
S1-SPS	81.4 (1.2)	3.3 (0.3)	0.9 (0.01)
S2	81.8 (1.2)	3.3 (0.3)	0.8 (0.02)
S2-SPS	81.8 (1.2)	3.3 (0.3)	0.9 (0.01)

Table S2: Mean and standard deviation (in parenthesis) values of the ^{27}Al MAS NMR parameters distribution obtained from fitted spectra shown in Fig. S4: isotropic chemical shift δ_{iso}, quadrupolar coupling constant C_Q and asymmetry parameter η.

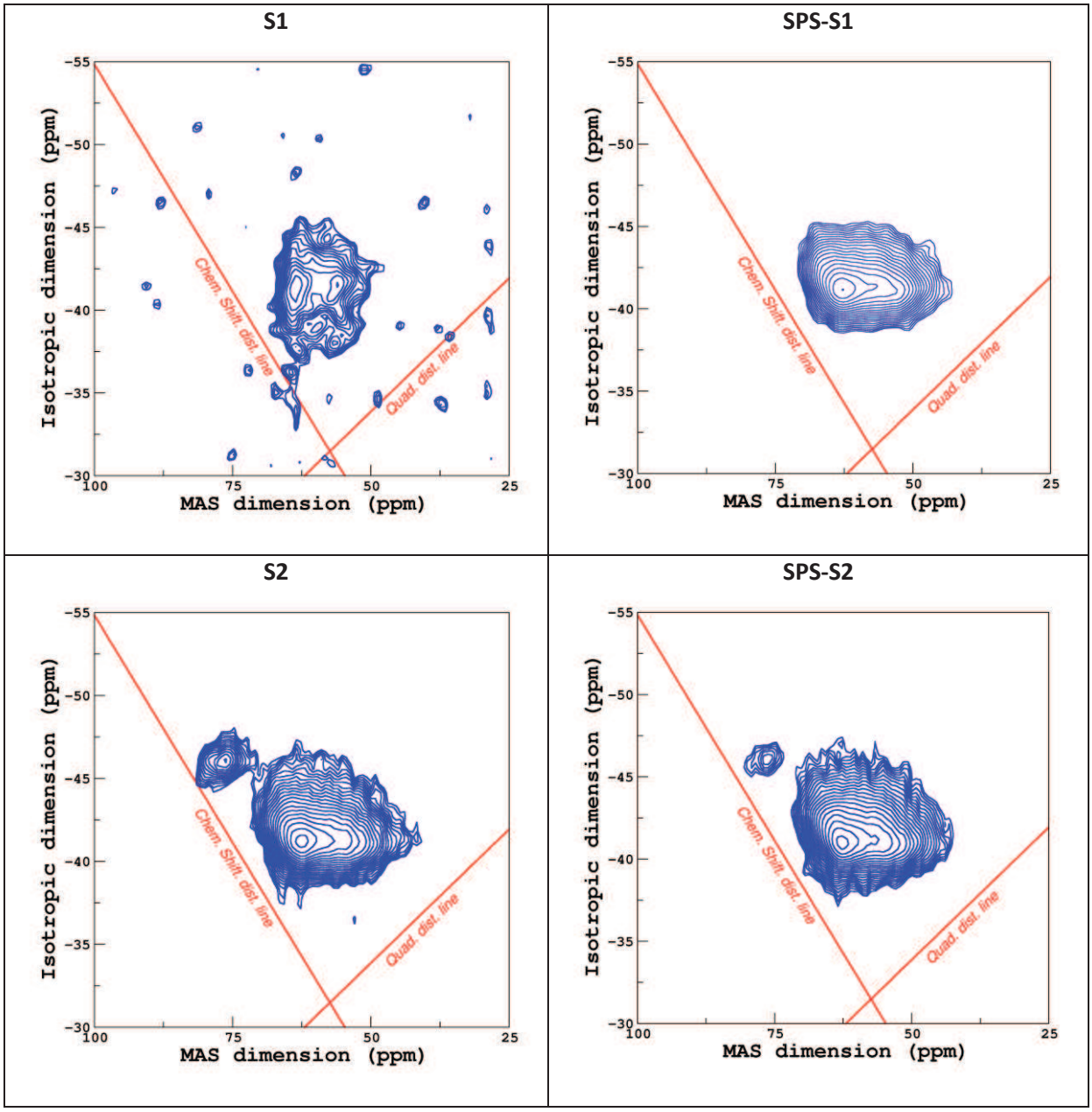

Fig. S5: Experimental ^{27}Al MQMAS NMR spectra of the studied samples at room temperature.

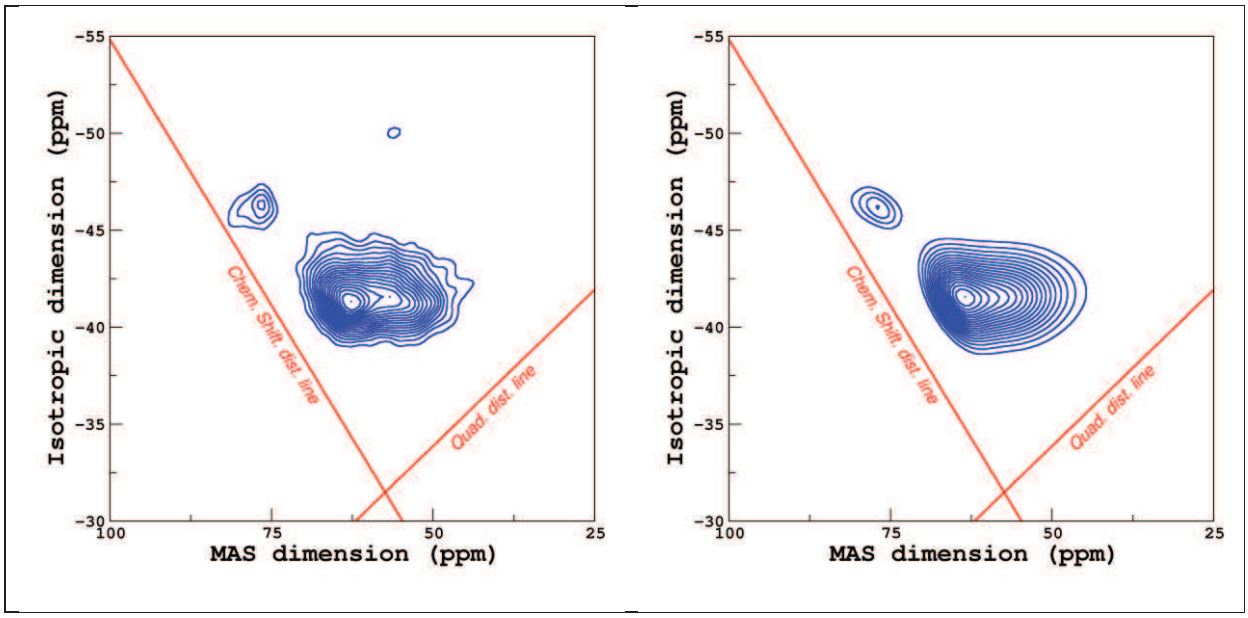

Fig. S6: Experimental (left) and simulated (right) ^{27}Al MQMAS spectra of S2.